

# Correlated X-ray/optical variability in the quasar MR 2251–178

P. Arévalo,<sup>1\*</sup> P. Uttley,<sup>1</sup> S. Kaspi,<sup>2,3</sup> E. Breedt,<sup>1</sup> P. Lira<sup>4</sup> and I. M. McHardy<sup>1</sup>

<sup>1</sup>*School of Physics and Astronomy, University of Southampton, Southampton SO17 1BJ*

<sup>2</sup>*School of Physics and Astronomy and the Wise Observatory, Raymond and Beverley Sackler Faculty of Exact Sciences, Tel Aviv University, Tel Aviv 69978, Israel*

<sup>3</sup>*Physics Department, Technion, Haifa 32000, Israel*

<sup>4</sup>*Departamento de Astronomía, Universidad de Chile, Casilla 36-D, Santiago, Chile*

## ABSTRACT

Emission from active galactic nuclei is known to vary strongly over time over a wide energy band, but the origin of the variability and especially of the interband correlations is still not well established. Here we present the results of our X-ray and optical monitoring campaign of the quasar MR 2251–178, covering a period of 2.5 years. The X-ray 2–10 keV flux is remarkably well correlated with the optical *B*, *V* and *R* bands, their fluctuations are almost simultaneous with a delay consistent with 0 d and not larger than 4 d in either direction. The amplitude of variations shows an intriguing behaviour: rapid, large amplitude fluctuations over tens of days in the X-rays have only small counterparts in the optical bands, while the long-term trends over hundreds of days are *stronger* in the *B* band than in X-rays. We show that simple reprocessing models, where all the optical variability arises from the variable X-ray heating, cannot simultaneously explain the discrepant variability amplitudes on different time-scales and the short delays between X-ray and optical bands. We interpret the variability and correlations, in the optically thick accretion disc plus corona scenario, as the result of intrinsic accretion rate variations modulating both X-ray and optical emission, together with reprocessing of X-rays by the accretion disc.

**Key words:** galaxies: active.

## 1 INTRODUCTION

Optical continuum variability is a universal property of radio-quiet active galactic nuclei (AGN) which has been studied for several decades, but its origin is still unclear. The optical continuum emission almost certainly originates from the accretion disc (Koratkar & Blaes 1999), so it is natural to assume that disc variability (e.g. through accretion rate fluctuations) drives the optical variability. Models where the variability is *intrinsic* to the disc, however, suffer from several problems. First, optical variability is seen on time-scales as short as a day, whereas accretion variability time-scales in standard accretion discs (Shakura & Syunyaev 1973) should be long in the optically emitting regions, comparable to the viscous time-scale which can be of the order of a year or more (Treves, Maraschi & Abramowicz 1988). Secondly, variations are well correlated in different optical bands, with only short (days) delays between bands, in the sense that longer wavelength variations lag shorter wavelength variations (Wanders et al. 1997; Collier et al. 2001; Cackett, Horne & Winkler 2007). Since local disc temperature  $T$  should decrease with radius  $R$  as  $T \propto R^{-3/4}$ , shorter

wavelengths originate from smaller radii. Therefore, in the case of inward-propagating fluctuations the long-wavelength variations lead, rather than lag, the short-wavelength variations. Furthermore, the resulting delays would be large, comparable to the radial drift time-scale, contrary to the observed day-scale delays.

To account for the observed optical properties, Krolik et al. (1991) suggested that the variability is driven by changes of the X-ray continuum which illuminates and thereby heats the disc, causing optical continuum variations. Since the X-ray emission is likely to be centrally concentrated, blue bands should respond to the X-ray variations first, followed by red, with short delays corresponding to the light-travel time delay between the blue- and red-emitting parts of the disc. The predicted optical time-delay  $\tau$  scales with wavelength  $\lambda$  as  $\tau \propto \lambda^{4/3}$  (Collier et al. 1999), and the observed dependencies of optical continuum lags on wavelength are consistent with this prediction (Cackett et al. 2007).

A more stringent test of reprocessing models is to directly compare X-ray and optical variations, using multiwavelength monitoring campaigns. To date, a handful of these campaigns have been carried out, largely facilitated by the *Rossi X-ray Timing Explorer* (*RXTE*) in conjunction with various ground-based observatories. The results have been mixed, with some AGN showing good evidence for correlated variability, as would be expected from

\*E-mail: patricia@astro.soton.ac.uk

reprocessing models (e.g. NGC 4051, Peterson et al. 2000; Shemmer et al. 2003; NGC 5548, Uttley et al. 2003; Mrk 509, Marshall, Ryle & Miller 2008), while others show more complicated but possibly correlated behaviour (e.g. NGC 7469, Nandra et al. 1998, 2000) and one AGN shows no apparent correlation at all (NGC 3516, Maoz et al. 2002).

The best case for correlated variability to date is NGC 5548, but Uttley et al. (2003) note that it is difficult to reconcile the large fractional amplitude of optical variability on time-scales of months–years with reprocessing models, since the X-ray variability shows smaller amplitude variations than the optical on these long time-scales. One would expect smaller relative variations in optical since the intrinsic emission due to viscous disc heating would dilute any variable reprocessed component. Furthermore, Gaskell (2008) notes that a simple energetic argument rules out reprocessing as the dominant source of optical variability in many AGN (including NGC 5548) which have ‘big blue bumps’ dominating the total luminosity, significantly exceeding the X-ray luminosity available for reprocessing. Detailed reprocessing calculations produced by Kazanas & Nayakshin (2001) for the case of NGC 3516 show that simple reprocessing of X-rays on their own could not produce the observed optical variability. Furthermore, in some AGN with simultaneous X-ray and optical monitoring, there is evidence that the optical may *lead* the X-ray variations, which might be expected if at least some of the optical variability is produced by intrinsic accretion fluctuations propagating through the disc (Shemmer et al. 2003; Marshall et al. 2008).

Clearly, no single model provides a satisfactory explanation for all the data. It is possible, however, that some combination of reprocessing and intrinsic accretion variations may explain the diverse range of optical/X-ray behaviour which is already observed in only a small sample of AGN. The location of the optical emitting region probably plays a key role in determining the balance of intrinsic versus reprocessed variability. It is governed by the disc temperature, which scales inversely with radius  $R$  (in units of the gravitational radius  $R_g = GM/c^2$ ) but also scales with black hole mass  $M_{\text{BH}}$  and accretion rate (as a fraction of the Eddington rate)  $\dot{m}$  as  $T \propto [(\dot{m}/M_{\text{BH}})R^{-3}]^{1/4}$  (Treves et al. 1988). Thus over the three decade range in black hole mass expected for AGN, we expect the radius corresponding to a given temperature to change by a factor of 10 (at the same fractional accretion rate), perhaps even more for different accretion rates. Since disc temperature governs the radius where peak optical emission is produced, Uttley et al. (2003) suggested that a diverse range of optical/X-ray behaviour might result from the range of masses and accretion rates expected in AGN (see also Li & Cao 2008). For example, the AGN with the most massive black holes will have cool discs and very centrally concentrated optical-emitting regions, in terms of gravitational radii. Therefore, the disc variability time-scales will be short, comparable with the X-ray variability time-scales, so intrinsic disc variability as well as reprocessing may contribute significantly to the optical variations. In contrast, AGN with lower mass black holes will have hotter discs so optical emission will originate from larger radii, where disc variability time-scales are very long compared to the corresponding time-scales in the innermost regions, so that only reprocessing may contribute significantly to the rapid variability we observe.

To test composite models of optical variability, it is necessary to carry out combined optical/X-ray monitoring of AGN with widely varying masses and accretion rates. To date, these campaigns have focused on Seyfert galaxies, which typically cover bolometric luminosities ranging from  $10^{43}$  to  $10^{45}$  erg s $^{-1}$ . Here we report the first optical/X-ray correlation for a more luminous radio-quiet AGN, the

quasar MR 2251–178 which we have monitored simultaneously in X-ray and optical bands for the past 2.5 years. We describe the data in Section 2 and show the cross-correlations in Section 3. In Section 4 we explore reprocessing and propagating fluctuations scenarios to explain the X-ray/optical variability in this source and discuss the implications of our results in Section 5.

## 2 DATA

MR 2251–178 was monitored in the X-ray band using the *RXTE* and in several optical bands with the 1.3-m SMARTS (Small and Moderate Aperture Research Telescope System) telescope in Chile and the 1-m telescope at the Wise Observatory. Below we give a brief description of the observational campaigns and the construction of the light curves.

### 2.1 X-ray monitoring with *RXTE*

We have monitored MR 2251–178 in the X-ray band with *RXTE* taking 1-ks exposure snapshot every 4.3 d. In the present paper, we include X-ray data from 2004 March 27 to 2008 January 13. Within this period, an intensive monitoring campaign was carried out with daily observations for three months, between 2007 August 2 and November 1.

Data were obtained using the *RXTE* Proportional Counter Array (PCA), which is sensitive in the range  $\sim 2.7$  to 60 keV and consists of five Proportional Counter Units (PCUs). Since PCU 0 has lost its xenon layer leading to a changed instrumental response and high background, and PCUs 1, 3 and 4 are regularly switched off for our observations, we only extracted data from PCU 2. We use standard good-time interval selection criteria (Earth elevation,  $\text{ELV} > 10^\circ$  and source pointing  $\text{OFFSET} < 0:02$ ). Background data were created using the combined faint background model and the SAA history file which are all current as of 2008 March. We extracted spectra in the 3–12 keV energy range for each snapshot and used *XSPEC* to fit a simple absorbed power-law model with the absorption column fixed at the Galactic value,  $N_{\text{H}} = 2.8 \times 10^{20}$  (Lockman & Savage 1995) to obtain an estimate of the 2–10 keV flux and its error. The top panel in Fig. 1 shows the resultant 2–10 keV flux light curve.

### 2.2 B- and V-band monitoring with SMARTS

We used the ANDICAM (A Novel Dual Imaging CAMera) instrument mounted on the 1.3-m SMARTS telescope in Cerro Tololo, Chile, to take images of MR 2251–178 in the *B* and *V* filters. The observational sampling was set up to match the *RXTE* monitoring, starting from 2006 August. Observations were taken every 4 d between 2006 August 3 and 2007 December 14, with a daily sampling period in 2007 from August 2 to November 1.

Two images were taken for each filter and observation date. We performed aperture photometry on MR 2251–178 and two nearby, non-variable, reference stars in the field of view, of similar flux to the target, using an aperture radius of 10 pixel = 3.7 arcsec. The typical full width at half-maximum (FWHM) of the observations was 1.5 arcsec. We confirmed that the relative flux of the reference stars was constant throughout the campaign. Relative flux light curves were constructed by dividing the flux of the MR 2251–178 by the combined measurement of both stars. In all cases where both nightly observations were good, we combined the relative fluxes, to produce one light curve point per night of observation. A sample *B*-band image is shown in Fig. 2; the target is marked by a circle

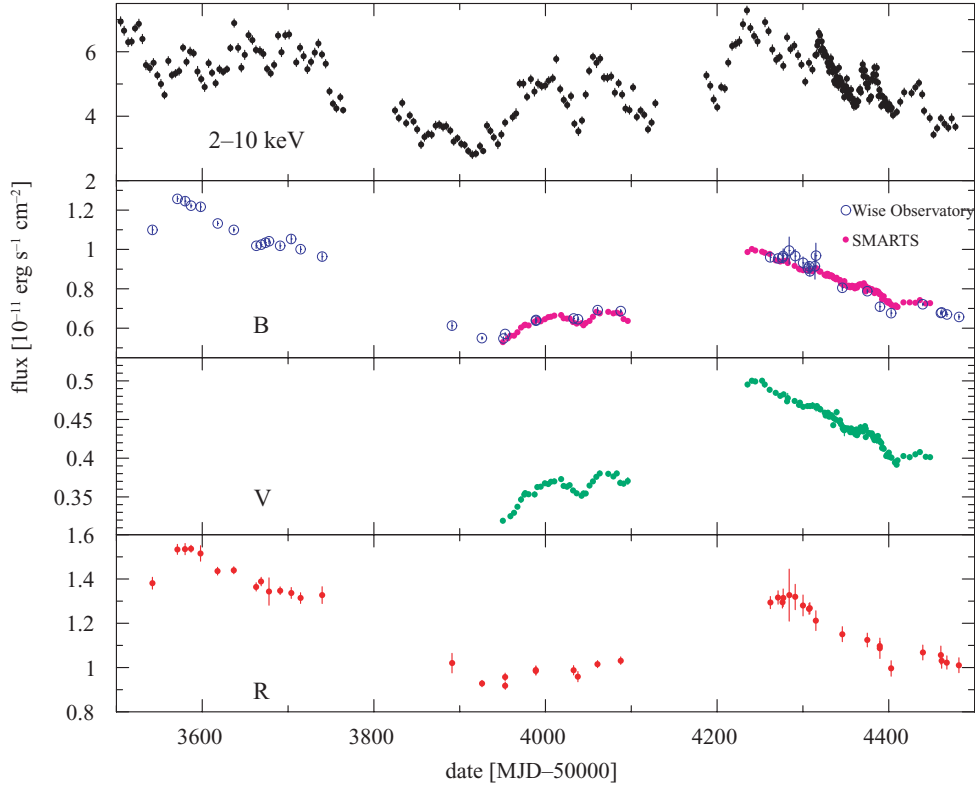


**Figure 1.** MR 2251–178 light curves. From top to bottom: 2–10 keV X-rays; *B*-band Wise Observatory data in blue open circles and *B*-band SMARTS data in pink filled circles; *V*-band SMARTS data, and *R*-band Wise Observatory data. The X-ray light curve is only shown for dates with optical band coverage. Gaps in the light curves correspond to the epochs when the source is not visible from the ground.

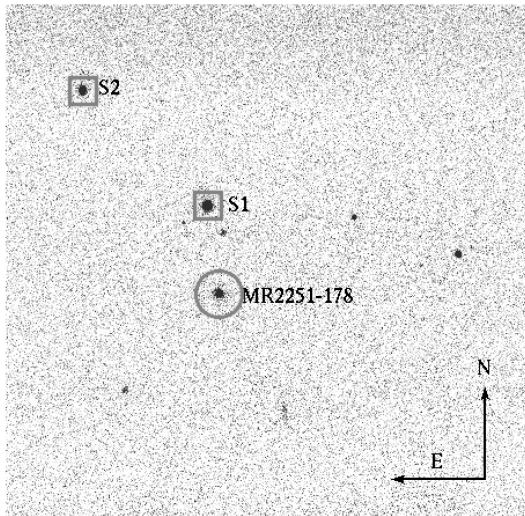


**Figure 2.** SMARTS field of view; the target MR 2251–178 and the two reference stars are labelled. The arrows pointing N and E are 1 arcmin long.

in the figure and both reference stars used are marked by squares and labelled S1 and S2. The source appears point like in our images and the extraction radius is large enough that changes in seeing produce a negligible effect in the measured flux. Using an aperture of 20 pixel produces an identical relative-flux light curve, with a flux offset of 3 per cent compared to the 10-pixel aperture radius light curve. Visual inspection of optical spectroscopic data obtained with the SMARTS 1.5-m telescope (not shown here) does not reveal

the presence of any absorption features that could correspond to the underlying stellar population, so we conclude that the galaxy contribution to the AGN flux is small.

### 2.3 Calibration of the optical light curves

The 1.3-m SMARTS telescope observed Landolt standards fields every photometric night during the campaign to produce zero-point magnitudes and extinction correction factors for each filter. We used these zero-points and correction factors, together with the airmass of our observations, to calculate the magnitude of our reference stars. For the calibration, we performed aperture photometry on our reference stars with 20-pixel aperture radius, to match the aperture used on the Landolt standards, although the resulting magnitudes were almost identical to the values using 10-pixel apertures. The resulting average values, using 151 photometric measurements for *B* and 153 for *V* were  $B = 14.00$  and  $V = 13.71$  for S1 and  $B = 14.90$  and  $V = 14.58$  for S2, with errors (rms/number of points) of 0.003 mag. We converted these magnitudes into fluxes at 5500 Å for the *V* band and 4400 Å for *B*, assuming a flat spectrum ( $\alpha = 0$ ) within each band. We averaged the fluxes of both stars and used this value to calibrate the flux light curves of MR 2251–178. The error bars on all optical light curves correspond to the error on the relative flux and were calculated by propagating the error on the photometry of MR 2251–178 and the comparison stars. We do not include the error on the calibration zero-point of the reference stars because an error in this quantity produces a shift by the same factor in all the data points and does not contribute to the point-to-point scatter in the light curves.

## 2.4 *B*- and *R*-band monitoring with the Wise Observatory

MR 2251–178 was monitored in the *B* and *R* optical bands between 2005 June and 2007 December, with observations approximately every two weeks up to 2006 December and then weekly for the rest of the campaign. The data reduction and light-curve extraction were done following the procedure described in Kaspi et al. (2007). As the field of view of these images is larger than in the SMARTS data, up to 11 non-variable reference stars could be used to create a relative flux light curve for MR 2251–178. We scaled the *B*-band relative flux light curve to match the SMARTS *B*-band data, over the periods of time where the light curves overlapped. To allow for differences in starlight contamination between the two light curves, possibly caused by the different apertures and average seeing, we fitted an additive offset as well as a relative normalization when matching the Wise Observatory to the SMARTS fluxes. The small best-fitting offset,  $6 \times 10^{-13} \text{ erg s}^{-1} \text{ cm}^{-2}$ , was added to Wise Observatory light curve. For the *R*-band calibration, we obtained the magnitudes of the reference stars S1 and S2 published in the US Naval Observatory catalogue (USNO V1) to correct the instrumental magnitudes and to convert these into observed fluxes. The published *R* magnitudes are 12.82 for S1 and 13.41 for S2. We used the calibrated flux of these reference stars to produce the light curve of MR 2251–178.

## 3 X-RAY/OPTICAL CROSS-CORRELATION

As a first step to compare the variability in different energy bands, we cross-correlated the light curves, using the discrete correlation function (DCF) method of Edelson & Krolik (1988) and the z-transformed cross-correlation function (ZDCF) as described in Alexander (1997). The DCF measures the degree of correlation between the two light curves as a function of time lag, i.e. displacement of one of the light curves on the time axis. A DCF value of 1 (–1) indicates completely (anti)correlated data, a value of 0 indicates the data are not correlated. Unless stated otherwise, a positive value of the time lag corresponds to X-rays leading.

We first compute the ZDCF between the complete X-ray and *B* light curves as this method can deal with sparsely sampled data. The resulting correlation function has a central peak reaching a maximum correlation coefficient of 0.71 at a lag of +9.6 d. This central peak is very broad, with correlation coefficient dropping to 0 at lags of –142 and +212 d. As is evident from the height of the ZDCF peak and from the light curves in Fig. 1, the long-term behaviour of the X-ray and optical bands are well matched, but it is hard to obtain an accurate lag. To determine the correlation on shorter time-scales, we split the light curves into year-long segments and calculated the DCF independently for each segment, avoiding the yearly gaps. We later combined the resulting DCFs weighting each segment by the number of DCF points contained. The third segment of the light curves covers the intensive monitoring campaigns in *B*, *V* and X-ray bands. We resampled the intensive light curves taking one point every 4 d, to match the observational rate of the rest of the campaign. This was done to give similar weighting to each similar-length segment and avoid letting the intensive sampling period dominate the combined DCF.

Fig. 3 shows the DCF between the X-ray and *B*-band light curves, calculated using the three segments shown in Fig. 1 and including Wise Observatory and SMARTS *B*-band data. The correlation has a broad central peak reaching a value of DCF = 0.64 (DCF = 0.72 for SMARTS data only) and a centroid lag of  $+3.6 \pm 9.3$  d. The centroid was calculated as the weighted average of lags with corresponding DCF values greater than 80 per cent of the maximum, within the

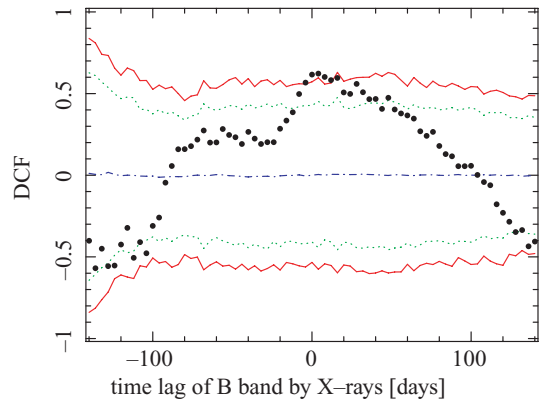


**Figure 3.** The DCF between the X-ray and *B* bands is plotted in black markers; positive lag values correspond to X-rays leading. The dotted lines represent the 95 per cent extremes of the distribution of simulated X-ray light curves when correlated with the real *B*-band light curve; the solid lines represent the 99 per cent extremes of this distribution. The correlation peak around time lag = 0 is significant above the 99 per cent significance level.

central peak. We prefer the centroid to the DCF peak lag because it is less sensitive to the particular DCF binning used. The lags and errors were estimated using the random sample selection method of Peterson et al. (2004), selecting randomly 67 per cent of the data points in the optical light curve together with their nearest X-ray data point and calculating the DCF centroid for 1000 such trials. The mean lag corresponds to the mean of the 1000 trial centroid lags and the error corresponds to the rms spread of the trial centroid lags. We repeated the calculation using *B*-band SMARTS data only and obtained a virtually identical DCF.

The X-ray light curve is equally well correlated with the *V* band. The DCF was calculated using the last two segments of the X-ray light curve and the corresponding segments of the SMARTS *V*-band data, which was also resampled to match the sampling frequency of the rest of the light curve. The central peak reaches DCF = 0.69 with a very similar shape and lag to the X-ray versus *B*-band case.

The DCF between X-ray and *R*-band data was calculated for the three light-curve segments shown in Fig. 1 and later combined. The resulting X-ray versus *R*-band DCF has a broad central peak reaching values of  $\sim 0.5$  between lags of –24 and +80 d. The mean centroid lag is 29 d but the error on the lag is not well constrained. The significance of all the correlations was estimated using a Monte Carlo method described in Section 3.1.

### 3.1 Testing the significance of the DCF

We simulated X-ray light curves, uncorrelated with the observed data, and calculated the DCF between them and the observed optical light curve. By repeating this process many times, we estimate the probability of obtaining by chance equal or higher DCF peaks than observed in the real data. We used the method of Timmer & König (1995) to produce red-noise light curves with a given underlying power spectrum to generate the simulated X-rays. The model power spectrum was chosen to be a single-bend power law of slope equal to –1 at low frequencies, bending to a steeper slope at high frequencies, using parameters that match the shape and normalization of MR 2251–178 X-ray power spectrum as measured by Summons et al. (in preparation). Light curve points were generated in bins of 0.1 d and for a length 10 times longer than the observed X-ray light curve, in order to allow for the long-term trends which

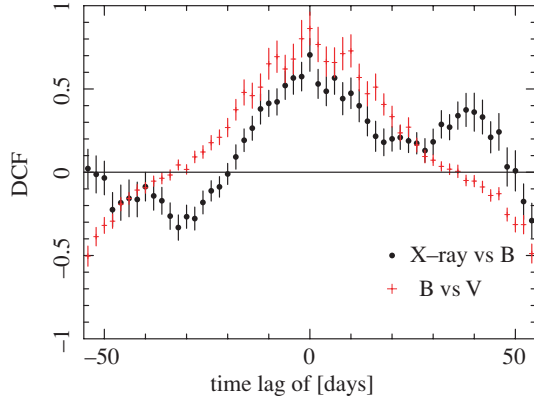


**Figure 4.** DCF calculated using the daily sampled light curves only (MJD 54300 to 54400) between X-ray and  $B$  band in black dots and between  $B$  and  $V$  bands in red crosses. The X-ray versus  $V$ -band DCF is very similar to the X-ray versus  $B$  band and is not shown for clarity. Positive lag values indicate higher energy band leading.

occur in red-noise data. The simulations were then sampled exactly as the real data and observational noise was added at the appropriate level. We calculated the DCF between these simulated light curves and the real optical data in the same way as was done with the real X-ray data. We repeated this process 2000 times, recording the DCF values. The mean, 95 and 99 per cent extremes of the distribution of simulated  $B/X$ -ray band DCFs are plotted in dot-dashed, dotted and solid lines, respectively, in Fig. 3. As shown in the figure, the central peak in the real data DCF reaches higher than 99 per cent of simulated, uncorrelated light curves. The same is true for the X-ray versus  $V$ -band DCF. In the case of X-ray versus  $R$  band, the DCF central peak reached the level of the top 95 per cent of the simulations, but did not reach the 99 per cent level. The  $R$ -band light curve, however, is almost identical to the corresponding Wise Observatory  $B$ -band light curve. Given that the total, Wise Observatory plus SMARTS,  $B$ -band light curve is significantly correlated with the X-rays, it is likely that the drop in significance in the X-ray versus  $R$  correlation is only due to the smaller number of  $R$  data points available.

### 3.2 Short time-scale variability

We used the intensively sampled data taken between MJD 54300 and 54400, to put tighter constraints on lags between the bands. The DCF between X-rays and  $B$  band and between  $B$  and  $V$  bands, of the intensive sampling data only, are shown in Fig. 4; they both show a clear central peak around a lag of 0 d. The error bars in the figure are the standard DCF errors described in Edelson & Krolik (1988). The DCF centroids obtained for the main peaks are  $0.6 \pm 3.1$  d between X-ray and  $B$ ,  $1.3 \pm 3.3$  d for X-ray versus  $V$  and  $0.5 \pm 2.4$  d between  $B$  and  $V$ . In all cases, positive lag values indicate higher energy band leading. All the lags are consistent with 0 d and are constrained to be less than  $\sim 4$  d in either direction. The errors on the lags were again obtained using the random sample selection method of Peterson et al. (2004).

### 3.3 Variability amplitudes

Fig. 5 shows the daily-sampled X-ray,  $B$ - and  $V$ -band light curves. The rapid X-ray fluctuations on time-scales of tens of days in the X-ray band have only small counterparts in the optical light curves,

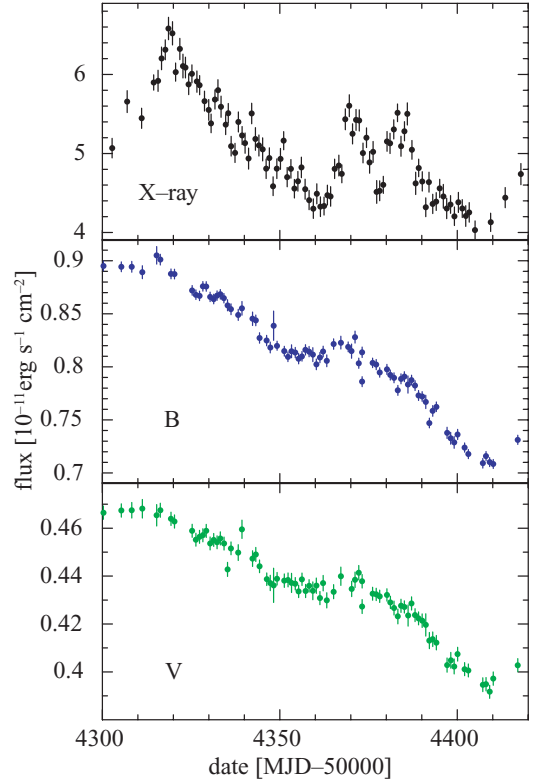
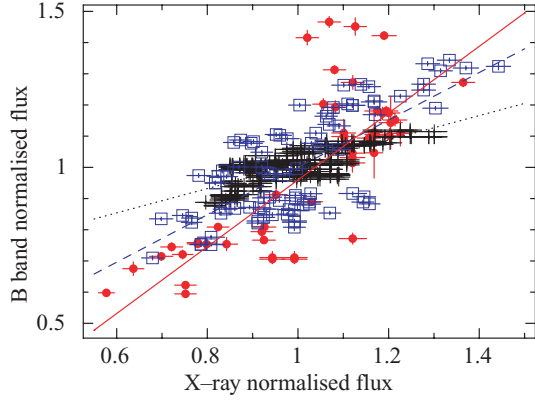


**Figure 5.** X-ray,  $B$  and  $V$  light curves covering the intensive monitoring campaign. The  $B$  and  $V$  fluxes have been calculated assuming an effective bandwidth of 968 Å for the  $B$  band and 880 Å for the  $V$  band.

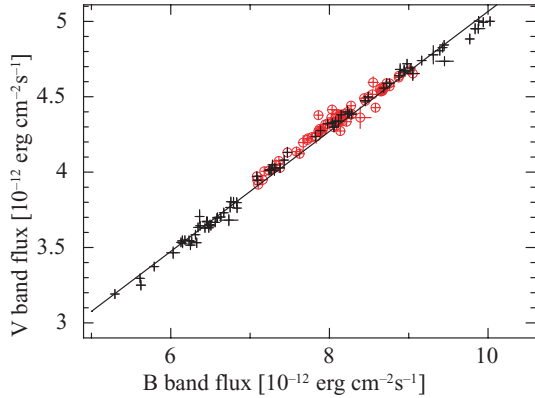
with a small or zero lag. As is clear from this figure and also Fig. 1, the long-term trends over hundreds of days appear in all bands. The relative amplitude of these long-term fluctuations is larger in the  $B$  band than in the X-rays: the minimum to maximum flux ratio observed in the X-rays for the entire period shown in Fig. 1 is 2.8, between the observations on MJD - 50000 = 3915 to 4234, while the SMARTS  $B$ -band data produce a ratio of 3.14 between days 3950 and 4240. An even larger flux ratio is shown on the period covered by the Wise Observatory data, when the  $B$ -band flux drops by a factor of 4 between 3571 and 3950.

Fig. 6 shows the  $B$ -band flux as a function of its nearest (less than 2 d apart) X-ray measurement, each normalized by the corresponding mean flux of the complete light curve. The dots correspond to the long-term,  $\sim 2$ -week sampled campaign covering 900 d, Wise Observatory data; the squares represent a shorter, 4-d sampling light curve covering 500 d and the crosses represent the intensive monitoring data, sampled daily for 90 d. The best-fitting linear relation for each data set gets flatter for shorter time-scales probed:  $B/\bar{B} = 1.07X/\bar{X} - 0.11$  for the long-term light curve (solid lines),  $B/\bar{B} = 0.76X/\bar{X} + 0.24$  for the intermediate (dashed line) and  $B/\bar{B} = 0.39X/\bar{X} + 0.62$  for the daily sampled, 90-d long light curve (dotted line). This change in slope shows how the  $B$  and X-ray light curves, although always correlated, have different time-scale behaviour, with rapid fluctuations being much stronger in the X-ray band and long-term trends being stronger in the  $B$  band.

The optical  $B$ - and  $V$ -band light curves from SMARTS are almost identical in shape and only differ in the amplitude of the fluctuations. Fig. 7 shows the  $V$  flux as a function of  $B$  flux for the same epoch, for the evenly 4-d sampled data and for the intensive monitoring sample, separately. The flux-flux plots are almost



**Figure 6.** Flux–flux plot of the X-ray and  $B$ -band data on different time-scales, for long (red dots), intermediate (blue squares) and short (black crosses) sampling patterns and light-curve lengths. The best-fitting linear relation for each data set gets flatter for shorter time-scales probed:  $B/\bar{B} = 1.07X/\bar{X} - 0.11$  for the long-term light curve (solid lines),  $B/\bar{B} = 0.76X/\bar{X} + 0.24$  for the intermediate (dashed line) and  $B/\bar{B} = 0.39X/\bar{X} + 0.62$  for the daily sampled, 90 d long light curve (dotted line).



**Figure 7.** Flux–flux plot of the SMARTS  $V$ - and  $B$ -band data; the crosses correspond to the 4-d sampling campaign and the open circles represent the intensive monitoring campaign. The flux in both bands varies almost proportionally, following a relation  $V = 0.4B + 1.09 \times 10^{-12} \text{ erg s}^{-1} \text{ cm}^{-2}$ , indicating that the  $B$  band varies proportionally more than the  $V$  band and that the latter contains a stronger constant offset.

linear, following a relation  $V = (0.398 \pm 0.005) B + (1.09 \pm 0.03) \times 10^{-12} \text{ erg s}^{-1} \text{ cm}^{-2}$  [ $\chi^2 = 137$  for 79 degrees of freedom (dof)] for the non-intensive segments, and  $V = (0.375 \pm 0.01) B + (1.31 \pm 0.09) \times 10^{-12} \text{ erg s}^{-1} \text{ cm}^{-2}$  ( $\chi^2 = 93.4$  for 73 dof) for the intensive sampling data. Notice that the short-term light curve has a slightly flatter flux–flux relation. Normalizing each light curve to its mean before computing the flux–flux relation produces the relative changes of flux in each band:  $V/\bar{V} = 0.75B/\bar{B} + 0.027$ , i.e. the relative amplitude of  $V$  fluctuations is smaller than in  $B$ . This difference in relative amplitude can be intrinsic to the variability process but it can also be partly due to starlight contamination producing a stronger constant component in the  $V$ - than  $B$ -band light curves.

The Wise Observatory  $B$  and  $R$  light curves are also well correlated following a linear relation of  $R = 0.83B + 4.6 \times 10^{-12} \text{ erg s}^{-1} \text{ cm}^{-2}$  shown in Fig. 8. Normalizing each light curve by its mean produces a relative variability relation of  $R/\bar{R} = 0.62B/\bar{B} + 0.38$ .

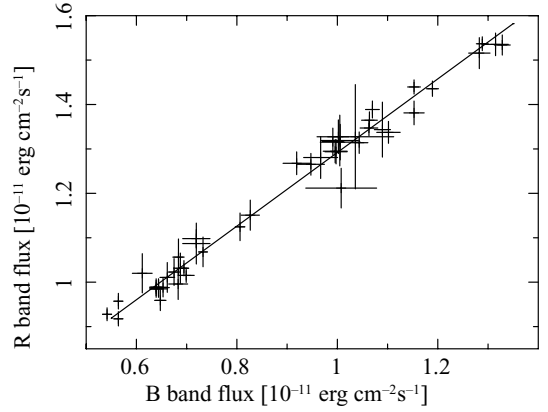


**Figure 8.** Flux–flux plot of the Wise Observatory  $R$ - and  $B$ -band data. The flux in both bands varies almost proportionally, following a relation  $R = 0.83B + 4.6 \times 10^{-12} \text{ erg s}^{-1} \text{ cm}^{-2}$ , indicating that the  $B$  band also varies proportionally more than the  $R$  band and that the latter contains a stronger constant offset.

## 4 THE ORIGIN OF THE CORRELATION AND LAGS

We have shown in the previous sections that the variability in the X-ray and optical  $B$ ,  $V$  and  $R$  bands is well correlated and that any time lag between optical and X-rays is small ( $< 4$  d). On time-scales of months, the fluctuations in the optical bands are similar to, and even larger than, the X-ray fluctuations while on shorter time-scales rapid, large amplitude X-ray flares have only small counterparts in the optical bands. In this section we will explore possible scenarios to explain the correlated variability between the bands.

### 4.1 Reprocessing

The small lags between optical and X-ray bands suggest their variations are connected through reprocessing of X-rays, possibly by an optically thick accretion disc, where the light travel time to the reprocessor is the main contributor to the time lags. This scenario could, in principle, also explain the lack of short time-scale fluctuations in the optical bands, as these can be smeared out by the finite light travel time to different parts of the reprocessor.

To test the predictions of this scenario, we generated thermally reprocessed light curves, using the observed X-ray light curves as input. We used the method described in Kazanas & Nayakshin (2001) to construct the reprocessed light curves. This model assumes a source of X-rays on the axis of symmetry of the system, illuminating the accretion disc from a height  $h$  in units of gravitational radii  $R_g = GM/c^2$ . The optical light curve is constructed by adding the X-ray flux received at each location in the disc, which depends on the X-ray source height, to the locally dissipated gravitational energy, as a function of radius. Each annulus in the disc is then assumed to emit this total flux as a blackbody so the characteristic temperature and flux in a given optical band can be calculated. The light travel time to the different parts of the accretion disc and from there to the observer are taken into account to produce the expected delays between X-ray and optical bands. We left the disc accretion rate  $\dot{m}$  as a free parameter, which governs the intrinsic, non-variable part of the optical flux.

The observed X-ray flux was converted to total luminosity assuming a distance of 271 Mpc to MR 2251–178, corresponding to its corrected redshift of  $z = 0.063$ , using  $H_0 = 73 \text{ km s}^{-1} \text{ Mpc}^{-1}$ ,

$\Omega_M = 0.27$  and  $\Omega_\Lambda = 0.73$ . We followed the X-ray spectral fitting of *BeppoSAX* data performed by Orr et al. (2001), to estimate the total (0.1–500 keV) X-ray flux incident on the disc and the reprocessed fraction. We considered a power-law model with reflection off cold material with a small reflection fraction  $R$ . A fit with XSPEC model PEXRIV, using  $R = 0.16$  and  $\xi = 465.1$  (Orr et al. 2001) produced a 0.01–500 keV flux of  $1.75 \times 10^{-10} \text{ erg s}^{-1} \text{ cm}^{-2}$ , while the 2–10 keV flux was  $4.64 \times 10^{-11} \text{ erg s}^{-1} \text{ cm}^{-2}$ . Therefore, we multiplied the 2–10 keV light curve by a factor of 4 to obtain the total incident X-rays. We also used the model fit to estimate the fraction of flux incident on a unit area of the thin disc which is absorbed, and therefore reprocessed into blackbody photons, obtaining a reprocessed fraction of 60 per cent.

The reprocessed optical light curves were scaled by the same distance of 271 Mpc to produce observed fluxes. We included an additional parameter  $A$  that multiplies the resulting optical flux to match the mean observed value. The function of this parameter is to absorb differences in predicted and observed fluxes due to uncertainties in the distance and extinction of the observed optical flux.

We varied  $h$ ,  $\dot{m}$ , black hole mass, inner truncation radius of the optically thick disc  $r_{\text{in}}$ , inclination angle to the observer  $\theta$  and rescaling factor  $A$  to try to reproduce the observed  $B$ -band light curve using the observed X-ray light curve as input. To first order, the effect of increasing  $h$  is to increase the lag between X-ray and reprocessed optical fluctuations and it also increases the disc covering fraction. The intrinsic disc accretion rate  $\dot{m}$  governs the stable disc flux, diluting the variability of the reprocessed component. Notice that the total optical luminosity depends on both  $\dot{m}$  and the inner truncation radius of the disc. The inclination angle introduces smoothing of reprocessed fluctuations since the response observed on the farther side of the disc lags the response of the nearer side by a maximum time of twice the light crossing time of the truncation radius, the maximum being produced when the disc is viewed edge-on. The black hole mass defines the size of the gravitational radius, so all the distances and therefore time-scales scale linearly with this parameter.

The model light curves corresponding to the best-fitting combinations of the parameters are shown in Fig. 9, together with the data for comparison. We first fitted each SMARTS  $B$ -band light curve segment separately. The best-fitting parameters for the first segment shown in Fig. 9 are  $h = 100R_g$ ,  $M = 10^9 M_\odot$ ,  $\dot{m} = 0.86$ ,  $r_{\text{in}} = 38R_g$ ,  $A = 0.15$ ; and for the second segment the parameters are  $h = 68R_g$ ,  $M = 4.5 \times 10^8 M_\odot$ ,  $\dot{m} = 0.38$ ,  $r_{\text{in}} = 30R_g$ ,  $A = 0.33$ , both with an edge-on view,  $\theta = 0.0$ . The high position of the X-ray source seems incompatible with an evaporating-disc corona but might correspond to the base of a weak jet. We applied each set of parameters to the other segment to produce the two pairs of reprocessed light curves, shown by the solid and dashed lines in the top panel of the figure. Clearly, the same set of model parameters cannot simultaneously reproduce the shapes of the two light-curve segments and their relative offsets, which are governed by long-term trends. Within a single segment, however, the model can reproduce the short-term behaviour moderately well. This result immediately suggests that, while the short-term fluctuations may be caused by reprocessing, the long-term variability should have a separate origin, e.g. as intrinsic accretion disc fluctuations.

To highlight the difficulty faced by simple reprocessing models in explaining the long-term optical variability, in the bottom panel of the figure we show a joint fit to both segments, with resulting parameters  $h = 100R_g$ ,  $M = 10^9 M_\odot$ ,  $\dot{m} = 0.58$ ,  $r_{\text{in}} = 83R_g$ ,  $A = 0.46$  and  $\theta = 0.0$ . The joint fit demonstrates that, in order to re-

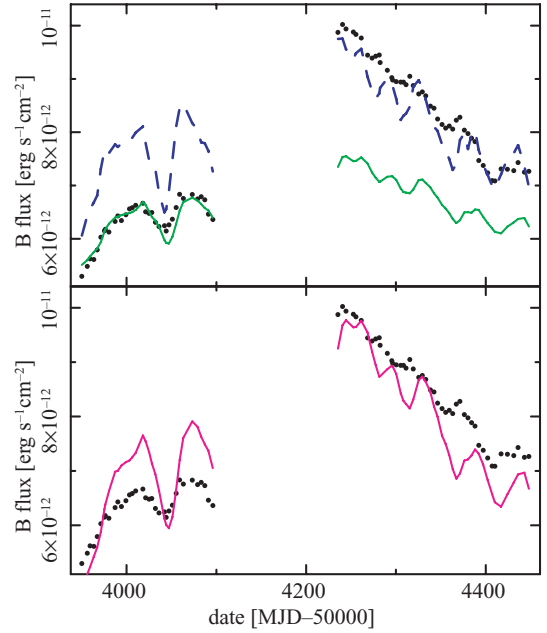


**Figure 9.** Reprocessing: the solid and dashed lines represent the reprocessed  $B$ -band light curves, calculated using the observed X-ray light curve as input. The dots represent the observed  $B$ -band light curve. In the top panel the reprocessing model has been fitted to only one segment at the time: the solid line corresponds to the fit to the first segment and the dashed line to the fit to the second. The solid line in the bottom panel shows the best fit to the two segments together.

produce the long-term fluctuations, the model necessarily produces too much rapid optical variability, even at an edge-on angle of observation which maximizes the smoothing. Additional smoothing is produced by having a larger reprocessor, i.e. pushing the inner truncation radius  $r_{\text{in}}$  outwards, but even then the model cannot smooth out the rapid fluctuations enough without introducing a noticeable optical to X-ray lag. Adding more intrinsic, constant, optical flux to reduce the short-term fluctuations does not solve this issue as this would also reduce the long-term trends, which are at least as strong in the  $B$  band as in X-rays. Therefore, X-ray reprocessing cannot be the sole cause of all the observed optical variability.

#### 4.2 Propagating fluctuations plus reprocessing

A possible origin for the long-term optical variability is fluctuations travelling through the accretion disc. In this scenario the X-ray and optical long-term trends can both be modulated by the accretion rate. A potential problem with this scenario is that if the accretion rate fluctuations propagate through a geometrically thin disc, their propagation time can be long and we would expect to see time lags between the bands, with lower energies *leading*. This problem can be circumvented if part of the X-rays is reprocessed by the disc. The large and rapid X-ray fluctuations can then produce some optical variability where the lower energy fluctuations will *lag*, therefore, cancelling part of the propagation effect.

We constructed a propagating-fluctuation model that includes reprocessing of the X-rays to test whether it can reproduce the different amplitudes of variability and correct time lags. We followed the prescription of Lyubarskii (1997), who proposes accretion rate fluctuations generated over a wide range in radii in the accretion disc, on the local viscous time-scale. The fluctuations propagate inward with viscous velocity through the disc and finally modulate

the X-ray emission at the centre. As the local time-scales decrease with radius, the more centrally concentrated emission contains the shortest time-scale fluctuations, seen especially in the X-rays. The resulting light curves for this model have a  $1/f$  power spectrum, bending to steeper slopes above a characteristic frequency, which is directly related to the shortest variability time-scales included, i.e. the viscous time-scale at the inner edge of the accretion flow. In a standard disc (Shakura & Syunyaev 1973), this characteristic time-scale is proportional to the mass of the black hole and is a function of the disc thickness ( $H/R$ ) and viscosity ( $\alpha$ ) parameters.

We incorporated reprocessing into the implementation of this model described in Arévalo & Uteley (2006), by adding an X-ray source above the disc and on the axis of symmetry. We assumed that the optical flux is emitted thermally by the disc with local emissivity proportional to the radial gravitational energy release. This emissivity profile is first modulated by the propagating accretion rate fluctuations and then also by the variable flux received from the X-ray source. We incorporate the travel time of the accretion rate fluctuations to the central X-ray emitting region and the light travel time of the X-rays to the different annuli in the accretion disc. For simplicity, only a face-on viewing angle was considered.

We used the observed X-ray flux and a distance of 271 Mpc as above, to obtain the X-ray luminosity. The black hole mass of MR 2251–178 has not been measured but, using the lower limit on the power spectrum break time-scale of Summons et al. (in preparation) and the relation between this quantity and black hole mass derived in McHardy et al. (2006), we derived a minimum mass of several times  $10^8 M_\odot$ . We fixed the mass of the black hole to  $8 \times 10^8 M_\odot$  and varied disc thickness and/or  $\alpha$  parameter to obtain the correct X-ray power spectrum from the simulated X-ray light curve, obtaining a value of  $(H/R)^2\alpha = 0.08$  at the innermost radius. As, in the model, the time-scales grow with black hole mass and decrease with  $\alpha$ , these parameters are largely degenerate so we only picked one set that fits the data but note that other pairs would work equally well. We then fixed these parameters and varied the height of the X-ray source and intrinsic mean disc accretion rate, to produce different realizations of the optical light curves.

One possible geometry for the accretion disc/corona system is a geometrically thin accretion disc that thickens towards the centre to produce a geometrically thick, optically thin corona. As the thickening of the flow produces shorter time-scale fluctuations at the same radius, the accretion rate that finally modulates the X-rays can have fluctuations on time-scales much shorter than the optical emission from the truncated thin disc. We kept the thickness to radius ratio  $H/R$  constant down to a truncation radius of  $r_t = 10R_g$ , with a value of  $(H/R)^2\alpha = 0.04$ , this produces viscous fluctuations up to time-scales of 300 d at the truncation radius. Inside  $r_t$ , we allowed  $H/R$  to grow with decreasing radius as  $(H/R)^2\alpha = 0.04(r_t/r)^{1.4}$  to reach the desired value of  $(H/R)^2\alpha = 0.08$  at  $r = 6R_g$  producing fluctuations on time-scales down to 5 d. We allowed the X-ray source to be higher than the top of the thick disc, but assumed that it was modulated by the thick flow fluctuations. The X-ray source height, however, had to be kept small at  $4-6R_g$  to produce sufficiently little reprocessing to reproduce the small relative size of the rapid optical fluctuations.

Fig. 10 shows 500 d long simulated light curves. The top panel represents the fluctuations in the innermost region, corresponding to the X-ray light curve, the bottom panel shows a  $B$ -band light curve modulated only by accretion rate fluctuations and the middle panel shows this same  $B$  light curve when the effect of reprocessing of X-rays is incorporated. As expected, the resulting X-ray and optical light curves are well correlated. Fig. 11 demonstrates the effects of

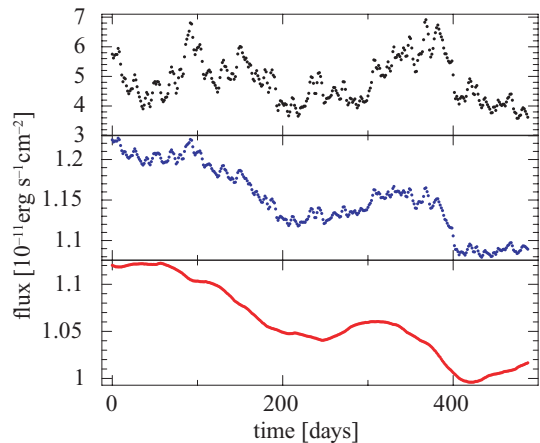


**Figure 10.** Simulated light curves of a propagating fluctuation model. The top panel represents the fluctuations in the innermost region, corresponding to the X-ray light curve. The bottom panel shows an accretion-disc emitted  $B$ -band light curve, modulated only by accretion rate fluctuations. The middle panel shows this same  $B$ -band light curve when the effect of reprocessing of X-rays is incorporated.

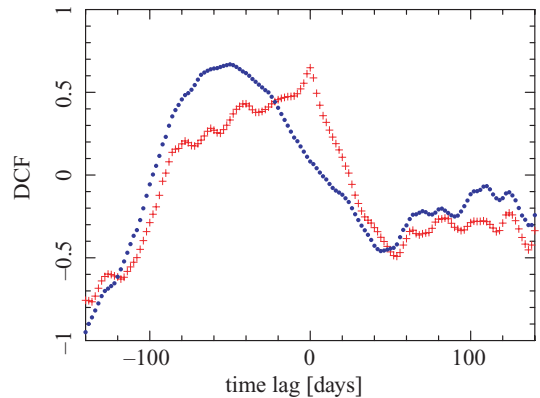


**Figure 11.** DCF between the simulated X-ray and  $B$ -band light curves shown in Fig. 10, including reprocessing of X-rays (crosses) and not including reprocessing (dots). The additional  $B$ -band fluctuations produced by reprocessing of X-rays move the DCF peak to 0 lag.

reprocessing on the DCF: the dots show the DCF between the simulated X-ray and  $B$ -band light curves if reprocessing is switched off (i.e. between the light curves shown in the top and bottom panels in Fig. 10), the  $B$  band leads the X-rays by approximately 50 d, which in this case is the travel time of the accretion fluctuations from the main  $B$  emitting region to the centre. If reprocessing is switched on, so that the rapid X-ray flares are imprinted as small optical fluctuations in the same light curve used above (shown in the middle panel of Fig. 10), the DCF peak shifts to a lag of 0 d, represented by the crosses in Fig. 11. The exact shape of the DCF between  $B$  and X-ray light curves changes with different realizations of the simulation even when exactly the same set-up and parameters are used. In Fig. 12 we show a few examples of such DCFs, calculated for different light-curve segments, each 500 d long. Given the changes in DCF peak height and direction of asymmetry, we cannot draw any conclusions from these structures in either the simulated or observed DCFs.

The amplitude of short-term fluctuations is strongly reduced in the optical compared to the X-rays and higher energy optical bands display larger variability than lower energy ones. The flux–flux



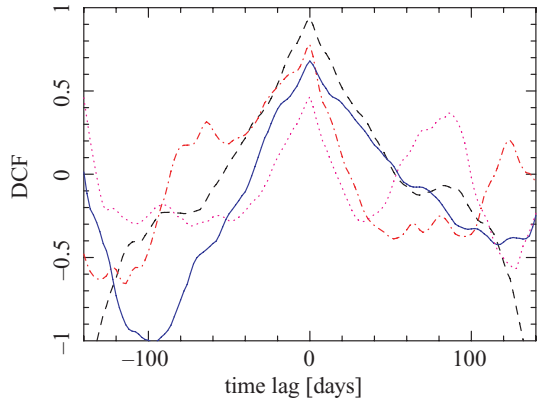


**Figure 12.** Sample of DCFs between different realizations of simulated X-ray and  $B$ -band light curves, with the same input parameters and length as those shown in Fig. 10. Here we plot the DCFs as continuous lines for clarity. The main DCF peak appears consistently around 0 lag but the height of the peak and the direction of its asymmetry depend on the realization.

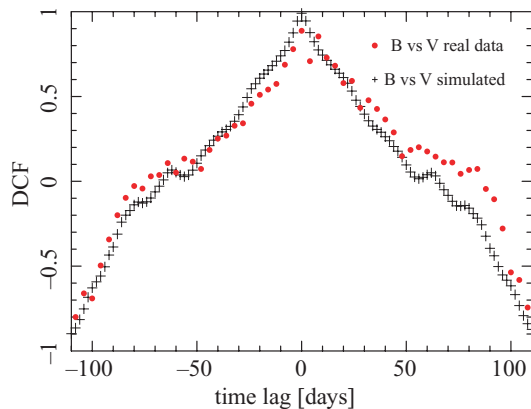


**Figure 13.** DCF between  $B$ - and  $V$ -band light curves for the real data (dots) and propagating fluctuation plus reprocessing simulated data (crosses).

relation of the simulated  $B$  and  $V$  light curves is similar to the real data, following a linear relation of the form  $V = 0.46B + 1.9 \times 10^{-12} \text{ erg s}^{-1} \text{ cm}^{-2}$ . In the model, the temperature radial profile of the accretion disc produces an emitting region that is more extended in the  $V$ - than in the  $B$  band, therefore, diluting more strongly in the  $V$ -band variability. This causes the lower variability amplitude in  $V$ , especially on short time-scales, without including any starlight contribution that might dilute the variability further.

The auto- and cross-correlation functions between optical light curves can also be reproduced. Fig. 13 shows the similarity of the DCFs between  $B$  and  $V$  bands of the real data and the simulated light curves shown in Fig. 10. These functions are almost symmetrical and very similar to the autocorrelation function, so we only display the DCFs for clarity. The simulations for this particular realization reproduce the right time-scale dependence of the variability and produce a lag between  $B$  and  $V$  light curves consistent with 0.

A feature which this simple implementation fails to reproduce is the larger amplitude of long-term optical fluctuations compared to the X-rays. This effect can appear for example if the fluctuations are damped as they propagate inward or as they transfer from the optically thick flow to the corona. As we only attempted a phenomenological approach to this fluctuating accretion model, we can easily introduce a damping parameter that reduces the X-ray long-

term fluctuations but this would not produce additional information on the physical processes involved.

## 5 CONCLUSIONS

We have carried out a simultaneous monitoring campaign in X-ray and optical  $B$ ,  $V$  and  $R$  bands on the quasar MR 2251–178 over 2.5 yr. All bands are significantly variable and their fluctuations are well correlated. The cross-correlation functions show peaks around a lag of 0 d, significant over the 99 per cent confidence level when compared to uncorrelated simulated data. All the delays between the bands are consistent with 0 d. We used daily sampled light curves in X-ray,  $B$  and  $V$  to constrain the lags between these bands, obtaining values of  $0.6 \pm 3.1$  d between X-ray and  $B$ ,  $1.3 \pm 3.3$  d for X-ray versus  $V$  and  $0.5 \pm 2.4$  d between  $B$  and  $V$  lags, where positive values indicate higher energy band leading. The lag between X-ray and  $R$  band was determined using the long but more sparsely sampled light curve, obtaining a value of  $-4.5 \pm 16.8$  d.

The long-term trends, over hundreds of days, are well matched by all the bands observed and are stronger in the  $B$  band than in X-rays, while the other optical bands show smaller amplitude trends. The optical light curves are not corrected by host galaxy contribution, however, so the decreased amplitude of variability in lower energy bands might be partly due to a constant galactic contribution. On short time-scales, of tens of days, there are large X-ray flares which appear strongly attenuated in the optical bands. The intensively sampled light curves show that the rapid X-ray flares do have optical counterparts, but that these are very weak.

Pure reprocessing of X-rays cannot produce both the short and long time-scale optical variability: if the long-term optical fluctuations were produced by reprocessing, we would expect similarly large rapid optical fluctuations, unless these could be smoothed by light travel effects. Any geometry of the reprocessor, however, cannot smooth out the fluctuations on time-scales of 20–50 d without introducing time lags of a similar length, which are not observed. A similar conclusion was reached by Kazanas & Nayakshin (2001) for the Seyfert galaxy NGC 3516, where the X-ray–UV variability could not be explained by simple reprocessing. We show that reprocessing of the observed X-rays cannot reproduce the optical variability in MR 2251–178, either producing rapid fluctuations that were too large or long-term trends that were too small. The short-term fluctuations however could be reproduced reasonably well with the model if we limited the light-curve lengths to  $\sim 100$  d, which reduces the contribution of long-term trends to each light-curve segment. Therefore, a moderate amount of reprocessing acting on an already long-term variable optical emission can reproduce the observed behaviour.

A simple way to decouple the amplitude of short- and long-term fluctuations is to have two distinct processes producing the optical variability, e.g. accretion rate fluctuations plus reprocessing. The covering fraction of the disc together with the ratio of intrinsic disc emission to X-ray heating determines the fraction of optical flux arising from reprocessed X-rays. Therefore, the size of the rapid optical fluctuations depends on these parameters and can be largely independent of the amplitude of the long-term trends. To test this possibility, we generated simulated light curves and compared their statistical properties with the observed data. In the model, fluctuations propagate inward through the accretion flow, modulating the optical emission as they travel through the thermally emitting region and finally modulate the X-ray emission, assumed to be located in the centre. This process leads to the long-term correlated variability. As the fluctuations are produced at every radius in the flow, on a

radially dependent time-scale, the centrally emitted X-rays contain short time-scale fluctuations which are originally absent in the optical light curves. The rapid fluctuations, only present in the X-ray emitting region are then introduced into the optical light curves through thermal reprocessing.

Lastly, although propagation times across the accretion disc can be long and produce a large lag between optical and X-ray fluctuations, reprocessing reduces the lag and can even revert it to a value of the order of the light crossing time to the reprocessor. For a black hole mass of  $10^9 M_{\odot}$  the light crossing time of one gravitational radius is 5000 s, so even for a large source height and inner truncation radius of  $50R_g$  the crossing time would be 4 d, less for a less massive black hole, which is within the observed limits on the lag. We show using the simulated light curves, that small-amplitude rapid fluctuations in the optical band can shift the CCF peak towards a lag of 0 d, even when the long-term trends of the optical lead the X-rays by  $\sim 50$  d. As inward propagation of the fluctuations and reprocessing have opposite effects on the time lag, the relative amount of optical/UV variability produced by each process determines the sign of the lag. This might be the case in other monitored AGN where the optical/UV can either lead or lag the X-rays.

An interesting feature of our fits to the optical variability is that we expect the disc to subtend a small solid angle with respect to the X-ray source, in order to reduce the effects of X-ray reprocessing and produce the correct amplitude of optical rapid fluctuations. This small solid angle is consistent with the small amount of reflection inferred from the broad-band X-ray spectrum of MR 2251–178 observed by *BeppoSAX* (Orr et al. 2001), which shows only a weak iron line with an equivalent width of  $EW \sim 70$  eV, and modest reflection continuum (reflected fraction  $< 0.4$ ). It is therefore possible that MR 2251–178 represents a source in a state where the thin disc is slightly truncated and/or the X-ray emitting region is at a small height over the disc. Optical/X-ray studies of other AGN should provide further useful constraints on their disc/corona geometries.

## ACKNOWLEDGMENTS

This work has made use of data obtained with *RXTE*, the SMARTS Consortium and the Wise Observatory telescopes. We wish to thank the SMARTS team for the good quality data obtained through their service mode observations. PA and IMM acknowledge support from STFC rolling grant PP/D001013/1 and PU from an STFC Advanced Fellowship. EB acknowledges support from a Stobie-SALT

Scholarship, from the South African NRF and the University of Southampton. PL acknowledges support from FONDECYT grant 1080603.

## REFERENCES

- Alexander T., 1997, in Maoz D., Sternberg A., Leibowitz E. M., eds, *Astrophys. Space Sci. Libr. Vol. 218, Astronomical Time Series*. Kluwer, Dordrecht, p. 163
- Arévalo P., Uttley P., 2006, *MNRAS*, 367, 801
- Cackett E. M., Horne K., Winkler H., 2007, *MNRAS*, 380, 669
- Collier S., Horne K., Wanders I., Peterson B. M., 1999, *MNRAS*, 302, L24
- Collier S. et al., 2001, *ApJ*, 561, 146
- Edelson R. A., Krolik J. H., 1988, *ApJ*, 333, 646
- Gaskell C. M., 2008, *Rev. Mex. Astron. Astrofis. Conf. Ser.*, 32, 1
- Kaspi S., Brandt W. N., Maoz D., Netzer H., Schneider D. P., Shemmer O., 2007, *ApJ*, 659, 997
- Kazanas D., Nayakshin S., 2001, *ApJ*, 550, 655
- Koratkar A., Blaes O., 1999, *PASP*, 111, 1
- Krolik J. H., Horne K., Kallman T. R., Malkan M. A., Edelson R. A., Kriss G. A., 1991, *ApJ*, 371, 541
- Li S.-L., Cao X., 2008, *MNRAS*, 387, L41
- Lockman F. J., Savage B. D., 1995, *ApJS*, 97, 1
- Lyubarskii Y. E., 1997, *MNRAS*, 292, 679
- McHardy I. M., Koerding E., Knigge C., Uttley P., Fender R. P., 2006, *Nat*, 444, 730
- Maoz D., Markowitz A., Edelson R., Nandra K., 2002, *AJ*, 124, 1988
- Marshall K., Ryle W. T., Miller H. R., 2008, *ApJ*, 677, 880
- Nandra K., Clavel J., Edelson R. A., George I. M., Malkan M. A., Mushotzky R. F., Peterson B. M., Turner T. J., 1998, *ApJ*, 505, 594
- Nandra K., Le T., George I. M., Edelson R. A., Mushotzky R. F., Peterson B. M., Turner T. J., 2000, *ApJ*, 544, 734
- Orr A., Barr P., Guainazzi M., Parmar A. N., Young A. J., 2001, *A&A*, 376, 413
- Peterson B. M. et al., 2000, *ApJ*, 542, 161
- Peterson B. M. et al., 2004, *ApJ*, 613, 682
- Shakura N. I., Syunyaev R. A., 1973, *A&A*, 24, 337
- Shemmer O., Uttley P., Netzer H., McHardy I. M., 2003, *MNRAS*, 343, 1341
- Timmer J., König M., 1995, *A&A*, 300, 707
- Treves A., Maraschi L., Abramowicz M., 1988, *PASP*, 100, 427
- Uttley P., Edelson R., McHardy I. M., Peterson B. M., Markowitz A., 2003, *ApJ*, 584, L53
- Wanders I. et al., 1997, *ApJS*, 113, 69